JOURNAL OF SPACECRAFT AND ROCKETS
Vol. 41, No. 6, November–December 2004

Hybrid Large-Eddy/Reynolds-Averaged Navier–Stokes Simulations of Shock-Separated Flows

Chen-Chuan Fan,* Xudong Xiao,† Jack R. Edwards,‡ and Hassan A. Hassan§
North Carolina State University, Raleigh, North Carolina 27695
and
Robert A. Baurle¶
NASA Langley Research Center, Hampton, Virginia 23681

An assessment of a hybrid large-eddy/Reynolds-averaged simulation (LES/RANS) procedure for high-speed, shock-separated flows is reported. A distance-dependent blending function is used to shift the turbulence closure from Menter's $k-\omega$ shear-stress-transport model near solid surfaces to a $k-\Delta$ subgrid closure away from solid surfaces and in free-shear regions. A modified recycling/rescaling procedure is used to generate time-dependent fluctuation data that are fed into the inflow plane for some calculations, with the goal being to replace the incoming boundary layer with a hybrid LES/RANS boundary layer that maintains nearly the same levels of fluctuation energy. Simulations of Mach 3 flow over a ramped-cavity configuration highlight the effects of grid refinement and choice of hybridization strategy, while simulations of Mach 3 flow over a 20-deg compression corner illustrate the effects of the choice of model constants and the inclusion of boundary-layer recycling on the mean-flow solutions.

Nomenclature

B	=	model constant
C	=	model constant
C_d	=	model constant
C_s	=	model constant
C_μ	=	model constant
d	=	distance to nearest wall, m
f	=	fluid property
$\bar{f}$	=	average fluid property
f''	=	fluctuating fluid property
k	=	fluctuation kinetic energy, m^2/s^2
$\tilde{l}_d$	=	turbulence length scale, m
P	=	pressure, Pa
P_k	=	turbulence production term, kg/(m-s^3)
T	=	temperature, K
t	=	time, s
u, v, w	=	Cartesian velocity components, m/s
u_τ	=	friction velocity, m/s
W	=	weighting function
x, y, z	=	Cartesian distance variables, m
β	=	ratio of friction velocities
β^*	=	model constant
Γ	=	blending function
Δ	=	filter width, m
δ	=	boundary-layer thickness, m
ϵ	=	dissipation rate, m^2/s^3
ζ	=	ratio of inverse timescales
η	=	inner-layer coordinate
μ	=	molecular viscosity, kg/(m-s)
ν	=	kinematic viscosity, m^2/s
ρ	=	density, kg/m^3
τ_1, τ_2	=	inverse timescale, s^{-1}
Ω	=	strain rate, s^{-1}
ω	=	turbulence frequency, s^{-1}

Subscripts

f	=	final
inl	=	inlet
inn	=	inner
out	=	outer
rec	=	recycle
w	=	wall
∞	=	freestream conditions

Presented as Paper 2003-0079 at the AIAA 41st Aerospace Sciences Meeting, Reno, NV, 6–9 January 2003 and Paper 2001-2929 at the AIAA 31st Fluid Dynamics Conference, Anaheim, CA, 11–14 June 2001; received 10 July 2003; revision received 2 December 2003; accepted for publication 2 December 2003. Copyright © 2003 by the American Institute of Aeronautics and Astronautics, Inc. All rights reserved. Copies of this paper may be made for personal or internal use, on condition that the copier pay the $10.00 per-copy fee to the Copyright Clearance Center, Inc., 222 Rosewood Drive, Danvers, MA 01923; include the code 0022-4650/04 $10.00 in correspondence with the CCC.

*Research Assistant, Department of Mechanical and Aerospace Engineering, Campus Box 7910. Student Member AIAA.
†Research Associate, Department of Mechanical and Aerospace Engineering, Campus Box 7910. Student Member AIAA.
‡Associate Professor, Department of Mechanical and Aerospace Engineering, Campus Box 7910. Senior Member AIAA.
§Professor, Mechanical and Aerospace Engineering, Campus Box 7910. Associate Fellow AIAA.
¶Aerospace Engineer, Hypersonic Airbreathing Propulsion Branch, Mail Stop 168. Senior Member AIAA.

Introduction

ALTHOUGH presumably more accurate than Reynolds-averaged Navier–Stokes (RANS) approaches, large-eddy simulation (LES) techniques are extremely expensive for high-Reynolds-number, wall-bounded flows, effectively precluding their use for many types of fluid-dynamic analysis. Hybrid simulation strategies,[1–18] which seek to combine RANS techniques in particular regions of a flowfield with LES techniques in other regions, offer one alternative to traditional LES and have received much recent attention. Particular successes have been achieved for external aerodynamic flows[5–7,13] or, more specifically, for flows in which there is a clear delineation between free-shear regions (typically treated as LES) and wall-bounded regions (typically treated as RANS).

The focus of this research is toward the development of improved procedures for computing unsteady turbulent flows characteristic of high-speed propulsive devices, such as scramjets and ramjets, which are being considered as key components for next-generation access-to-space launch vehicles. Within such devices, recessed cavities can be used to provide flame stabilization. Depending on the size and flow condition, such cavities can demonstrate large-scale unsteadiness, sustained by reflections of pressure waves from the cavity

walls. This represents a difficult situation to analyze using conventional RANS approaches, as the large levels of eddy viscosity produced in the free shear layer over the cavity can suppress the unsteadiness. Multiple shock-wave/boundary-layer interactions also occur within such devices, both within the inlet and within the isolator region, where a moving shock train can be established in response to combustion-induced heat release. The accurate prediction of single shock-wave/boundary-layer interactions is a major challenge for RANS turbulence modeling, and multiple interactions remain to be successfully predicted.

The present work develops a zonal hybrid LES/RANS procedure for analyzing such flowfields. In contrast to some hybrid methods, which depend on ratios of a grid scale to a local turbulence length scale to decide whether a region is to be treated as RANS or LES, a zonal approach allows for certain regions of the flow to be handled as LES and others as RANS in a manner more independent of the local grid spacing (provided that it is sufficient to resolve details of the large-eddy structure). The zonal decomposition can be done either in a predetermined manner[14,15] or in a flow-dependent manner.[16–18] The zonal method presented in this work uses a blending function similar to that found in Menter's hybrid $k-\epsilon/k-\omega$ RANS model[19] to shift the model from RANS behavior near solid surfaces to LES behavior further away. The model is applied to Mach 3 flow over the ramped-cavity configuration of Settles et al.[20,21] and to Mach 3 flow over a 20-deg compression corner.[22,23] The sections that follow present the turbulence closures tested in this work, boundary condition information, the numerical algorithm, and some results for the configurations just mentioned.

Turbulence Closure

One view[2] of the use of RANS ideas in essentially LES formulations is that they function as a sophisticated subgrid closure but one restricted in scope as a result of calibration for statistically stationary flows. In this work, we utilize Menter $k-\omega$ shear-stress transport (SST) model[19] as the RANS component of the closure. Menter's model reduces to a $k-\omega$ model near solid surfaces but shifts to a $k-\epsilon$ model away from solid surfaces. This shifting is accomplished through a blending function Γ dependent on the distance from the nearest wall d. The SST modification replaces the turbulence frequency ω in the eddy viscosity definition with a quantity proportional to the strain rate in regions where the strain rate can exceed the turbulence frequency. This can occur near solid surfaces, in the vicinity of strong shock waves, and in regions of flow separation and reattachment. The eddy viscosity is thus lowered in these regions, generally leading to more flow separation than predicted by the baseline Menter model.

The hybrid LES/RANS model utilizes a blending function Γ, dependent on the distance from the nearest wall d, to shift the closure from Menter's $k-\omega$ model near the wall to a one-equation subgrid model away from walls. The particular form chosen for the turbulence kinetic energy equation is as follows:

$$\rho\frac{\mathrm{D}k}{\mathrm{D}t} = P_k - \rho\left[\Gamma\beta^* k\omega + (1-\Gamma)C_d\frac{k^{\frac{3}{2}}}{\Delta}\right] + \frac{\partial}{\partial x_j}\left[(\mu+\mu_t)\frac{\partial k}{\partial x_j}\right] \tag{1}$$

and the eddy viscosity is given by

$$\mu_t = \rho\left[\Gamma(k/\omega) + (1-\Gamma)C_s\sqrt{k}\Delta\right] \tag{2}$$

In these expressions, P_k is the turbulence production term, which is approximated as

$$P_k = \mu_t\left[\left(\frac{\partial u_i}{\partial x_j}+\frac{\partial u_j}{\partial x_i}\right)\frac{\partial u_i}{\partial x_j} - \frac{2}{3}\frac{\partial u_k}{\partial x_k}\frac{\partial u_k}{\partial x_k}\right] \equiv \mu_t\Omega^2 \tag{3}$$

β^* is a constant appearing in Menter's model,[19] C_s and C_d are model coefficients, and Δ is a filter width defined as the cube root of the local cell volume. In the limit of balancing subgrid production and dissipation, the preceding model returns a Smagorinsky-type subgrid eddy viscosity: $\nu_t = C_s\sqrt{(C_s/C_d)}\Delta^2\Omega$. The value for C_s is chosen as 0.01 in this study, while C_d is assigned values of 0.01 and 0.1 in two simulations. These choices are different from those used in the Yoshizawa and Horiuti[24] one-equation subgrid model ($C_s = 0.05$; $C_d = 1.0$). The Yoshizawa choices were found to be consistently too dissipative when used with the present upwind methods, leading to insufficient eddy growth.

The blending function Γ is a modification of that initially presented in Ref. 19:

$$\Gamma = \tanh(\zeta^4) \tag{4}$$

$$\zeta = \max(\tau_1, \tau_2)/\omega \tag{5}$$

$$\tau_1 = 500\nu/d^2 \tag{6}$$

$$\tau_2 = \sqrt{k}\big/C_\mu d \tag{7}$$

where d is the distance from the nearest wall. The turbulence frequency ω is obtained from its transport equation as presented in Ref. 19, which is formulated so that its production term does not depend on the eddy viscosity. Thus, the ω equation is only weakly influenced by the changing eddy viscosity and turbulence kinetic energy as the model shifts from RANS to LES mode. The effect of the blending function is as follows. When the blending function is unity in Eqs. (1) and (2), the RANS component dominates, whereas the LES component dominates when the blending function is zero. All constants appearing in the modified blending function and in Menter's model are the same as defined as in Ref. 19.

The hybrid LES/RANS methods presented in Strelets et al.[4] and Bush and Mani[7] also use Menter's model as their basis. The shift to LES mode for these models is accomplished in different ways. Both rewrite the dissipative term in the k equation $\beta^* k\omega$ as $k^{3/2}/\tilde{l}_d$, where

$$\tilde{l}_d = \min\left[k^{\frac{1}{2}}\big/(\beta^*\omega), C\Delta\right] \tag{8}$$

with C being a model constant. Reference 7 also redefines the eddy viscosity as follows:

$$\mu_t = \rho\min\left(k/\omega, CC_\mu\sqrt{k}\Delta\right) \tag{9}$$

The model of Bush and Mani is closest to the present work, except that the shift from RANS to LES in the present work is accomplished through a (smoother) blending function that also directly involves the distance from the nearest wall.

The values of C_s and C_d in Eqs. (1) and (2) were arrived upon as a consequence of two competing requirements: availability of enough modeled turbulence energy to allow the blending function to shift from RANS to LES at the proper location and reduced eddy viscosity levels in the LES region, comparable to those produced by a Smagorinsky model. Lower values of C_d (for fixed C_s) tend to raise subgrid turbulence kinetic energy levels. This has the effect of pushing the RANS/LES juncture as provided by the blending function further away from solid surfaces, as a result of an increase in τ_2 in Eq. (7). Higher subgrid turbulence kinetic energy levels do not necessarily translate into higher subgrid viscosities, as seen if one takes the substantial derivative of the subgrid eddy viscosity definition $\nu_t = C_s\sqrt{(k)}\Delta$:

$$\frac{\mathrm{D}\nu_t}{\mathrm{D}t} = \frac{C_s}{2}\left(C_s\Delta^2\Omega^2 - C_d k\right) \tag{10}$$

It is clear from this equation that k actually acts as a destruction term for subgrid eddy viscosity. In LES regions, the resolved-scale contributions to the turbulence energy will dominate; thus, possible errors incurred by higher values of the subgrid turbulence energy (relative to the Yoshizawa model and others) should be minor.

The monotonically integrated large-eddy simulation (MILES) technique of Boris et al.[25] is also tested for one of the cases presented. In MILES, the eddy viscosity is set to zero, and the role of a subgrid closure is mimicked by the intrinsic dissipation inherent in the numerical scheme. The grids used in this study are too coarse in

the spanwise and streamwise directions to be considered suitable for a true LES in the near-wall regions. Thus, the MILES simulations considered herein are "very large-eddy simulations" in the sense used by Fureby and coworkers.[26]

Recycling Procedure

The compression-ramp flow discussed later presents a rigorous challenge to the zonal LES/RANS methods, as a clear delineation between regions modeled through RANS techniques and those modeled through LES is not obvious. For this case, it was found necessary to impose inflow boundary conditions that more accurately simulate the passage of organized turbulence structures into the domain. The approach used is a recycling procedure similar to that of Urbin et al.,[27] in which time-dependent fluctuation data are continuously fed into the inflow plane of the computational domain. The goal is to replace the incoming boundary layer (initially obtained from a RANS solution) with a time-dependent hybrid LES/RANS boundary layer that maintains nearly the same levels of fluctuation energy. A brief description of the procedure is presented next. Further details can be found in Refs. 18 and 27.

A schematic of the recycling procedure is shown in Fig. 1. The instantaneous flow properties are extracted from a plane approximately 0.1 m downstream of the inflow plane at each time step. They are decomposed into time mean parts $\bar{f}(x, y, z)$ and time-fluctuating parts $f''(x, y, z, t)$ according to

$$\bar{f} = \frac{1}{t_f - t_i}\int_{t_i}^{t_f} f\,\mathrm{d}t, \qquad f'' = f - \bar{f} \tag{11}$$

For the three velocity components (u, v, w), their fluctuating parts are recycled and rescaled to the inflow plane according to

$$\begin{aligned} u''^{\mathrm{inn}}_{\mathrm{inl}} &= \beta u''_{\mathrm{rec}}\left(y^+_{\mathrm{inl}}, z, t\right), & u''^{\mathrm{out}}_{\mathrm{inl}} &= \beta u''_{\mathrm{rec}}(\eta_{\mathrm{inl}}, z, t) \\ v''^{\mathrm{inn}}_{\mathrm{inl}} &= \beta v''_{\mathrm{rec}}\left(y^+_{\mathrm{inl}}, z, t\right), & v''^{\mathrm{out}}_{\mathrm{inl}} &= \beta v''_{\mathrm{rec}}(\eta_{\mathrm{inl}}, z, t) \\ w''^{\mathrm{inn}}_{\mathrm{inl}} &= \beta w''_{\mathrm{rec}}\left(y^+_{\mathrm{inl}}, z, t\right), & w''^{\mathrm{out}}_{\mathrm{inl}} &= \beta w''_{\mathrm{rec}}(\eta_{\mathrm{inl}}, z, t) \end{aligned} \tag{12}$$

where the superscripts inn and out denote the inner and outer regions of the boundary layer, respectively. The subscripts inl and rec represent the inlet and recycle stations, respectively; y^+ is the classical law of the wall coordinate ($y^+ = yu_\tau/\nu_w$), and it is used as the inner layer coordinate; η is defined as $\eta = y/\delta$, and it is used as the outer-layer coordinate. β is the ratio of the friction velocity at the inlet station to that at the recycle station:

$$\beta = u_{\tau,\mathrm{inl}}/u_{\tau,\mathrm{rec}} = (\delta_{\mathrm{rec}}/\delta_{\mathrm{inl}})^{\frac{1}{10}} \tag{13}$$

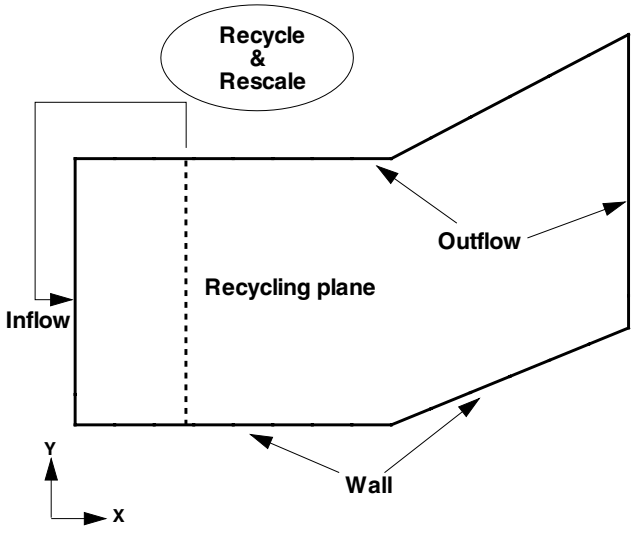

Fig. 1 Schematic of recycling procedure.

where

$$\frac{\delta_{\mathrm{rec}}}{\delta_{\mathrm{inl}}} = \left[1 + \left(\frac{x_{\mathrm{rec}} - x_{\mathrm{inl}}}{\delta_{\mathrm{inl}}}\right)0.27^{\frac{6}{5}}\,Re_{\delta_{\mathrm{inl}}}^{-\frac{1}{5}}\right]^{\frac{5}{6}} \tag{14}$$

The fluctuating temperature is recycled similarly, but without the ratio of friction velocity:

$$T''^{\mathrm{inn}}_{\mathrm{inl}} = T''_{\mathrm{rec}}\left(y^+_{\mathrm{inl}}, z, t\right), \qquad T''^{\mathrm{out}}_{\mathrm{inl}} = T''_{\mathrm{rec}}(\eta_{\mathrm{inl}}, z, t) \tag{15}$$

The new fluctuating profiles for velocity and temperature at the inflow are then obtained by forming a weighted average of the inner and outer profiles:

$$f''_{\mathrm{inl}} = f''^{\mathrm{inn}}_{\mathrm{inl}}[1 - W(\eta_{\mathrm{inl}})] + f''^{\mathrm{out}}_{\mathrm{inl}}W(\eta_{\mathrm{inl}}) \tag{16}$$

where f can be substituted with u, v, w, or T. The weighting function W is defined as

$$W(\eta) = \frac{1}{2}\left\{1 + \frac{1}{\tanh(4)}\tanh\left[\frac{4(\eta - B)}{(1 - 2B)\eta + B}\right]\right\} \tag{17}$$

where $B = 0.2$ to provide a smooth transition at $y/\delta = 0.2$. The new inflow profiles are then obtained by superimposing the recycled fluctuating components onto the mean components, which are extracted from the initial RANS solution and remain fixed throughout the hybrid simulation. This is the major difference between the current approach and that of Urbin et al.,[27] in which both mean and fluctuating components are rescaled and recycled. Other minor differences are described more completely in Ref. 18.

The turbulence quantities k and ω are also decomposed into time mean and time fluctuating parts. Unlike the velocity and temperature fields, both mean and fluctuating parts of the turbulence quantities are recycled and rescaled. They are recycled to the inlet according to

$$\begin{aligned} \bar{f}^{\mathrm{inn}}_{\mathrm{inl}} &= \bar{f}_{\mathrm{rec}}\left(y^+_{\mathrm{inl}}, z, t\right), & \bar{f}^{\mathrm{out}}_{\mathrm{inl}} &= \bar{f}_{\mathrm{rec}}(\eta_{\mathrm{inl}}, z, t) \\ f''^{\mathrm{inn}}_{\mathrm{inl}} &= f''_{\mathrm{rec}}\left(y^+_{\mathrm{inl}}, z, t\right), & f''^{\mathrm{out}}_{\mathrm{inl}} &= f''_{\mathrm{rec}}(\eta_{\mathrm{inl}}, z, t) \end{aligned} \tag{18}$$

where f represents either k or ω. The new profiles at the inflow are then obtained by an expression similar to Eq. (10):

$$f_{\mathrm{inl}} = \left(\bar{f}^{\mathrm{inn}}_{\mathrm{inl}} + f''^{\mathrm{inn}}_{\mathrm{inl}}\right)[1 - W(\eta_{\mathrm{inl}})] + \left(\bar{f}^{\mathrm{inn}}_{\mathrm{inl}} + f''^{\mathrm{out}}_{\mathrm{inl}}\right)W(\eta_{\mathrm{inl}}) \tag{19}$$

where the weighting function is the same as in Eq. (17).

Numerical Algorithm

The numerical approach for solving the hybrid LES/RANS system is essentially the same as presented in Ref. 28 for two-dimensional LES simulations of reactive hydrogen jets. The compressible Navier–Stokes equations are formulated in a generalized coordinate system. Second-order essentially nonoscillatory upwind methods[29] based on the low-diffusion flux-splitting scheme of Edwards[30] are used to discretize the inviscid components of the equation system, while central differences are used for viscous and diffusive terms. Time integration is facilitated by a planar relaxation subiteration procedure, which results in second-order temporal accuracy with sufficient subiteration convergence. Though not invoked in the present work, the code allows for arbitrary numbers of chemically reacting species. Differences between the present algorithm and that of Ref. 28 include an extension to three dimensions, the use of multiblock grids, and the inclusion of hybrid turbulence closure strategies. The code is parallelized using domain-decomposition/message-passing-interface (MPI) methods and is optimized for operation on the 720 processor IBM SP-2 at the North Carolina Supercomputing Center. Jacobian matrix elements are stored over the number of blocks mapped to a particular processor, allowing the "freezing" of the matrix elements and their factorization over the duration of the subiterations and even over several physical time steps. This reduces the computational workload significantly.

Experimental Accuracy

The experiments simulated in this work[20–23] were carried out in the Princeton University 20 × 20 cm high-Reynolds-number supersonic wind tunnel during the late 1970s and early 1980s. Pitot- and static-pressure measurements are estimated to be within ±2 and ±4%, respectively, with the static-pressure uncertainty increasing to ±10% near reattachment. The measurement of the stagnation temperature is assigned an error of ±6%. The reduction of this data into velocity and Mach-number profiles is assumed to have errors of ±5 and ±4%, respectively. Error bounds for Preston tube skin-friction measurements are not given in the archival references. Later reviews of some of this data indicate that probe-alignment effects could cause errors of up to 30% near shock waves. For the compression-corner configuration, it is difficult to assess the quality of the data in the vicinity of the ramp apex because of large-scale, low-frequency oscillations of the separation shock. This effect, although well-recognized today, was not investigated systematically in these early experiments. The cited references provide further details of the experimental configurations and error estimates.

Results

Simulations presented in this paper focus on two cases: Mach 3 flow past a ramped cavity[20,21] and Mach 3 flow over a 20-deg compression corner.[22,23] The results presented in this paper are synthesized from two earlier references.[16,17] The interested reader is encouraged to consult these references for complete details of the studies.

Ramped-Cavity Configuration

Figure 2 shows an X–Y cut of the three-dimensional grid of this configuration. The baseline grid consists of two blocks, containing 37 × 85 × 33 points upstream of the cavity and 165 × 125 × 33 points downstream of the leading edge of the cavity. The grid extends 0.0381 m in the Z direction and is clustered to all solid surfaces and in the vicinity of the reattachment location. A refined grid, containing twice as many points in the X direction downstream of the cavity leading edge, was used for selected calculations. Inflow conditions were obtained by calculating two-dimensional flow over a flat plate until the boundary-layer properties just upsteam of the cavity matched the experimental values. The nominal inflow Mach number, pressure, and temperature are 2.92, 21,240 Pa, and 95.37 K, respectively. Initial conditions for the hybrid simulations were obtained by solving the flowfield in two dimensions using the Menter SST model.

For the calculations presented, supersonic inflow boundary conditions were enforced just upstream of the cavity leading edge, with the velocity fields forced randomly according to a procedure presented in Ref. 28. This procedure ensures that the generated fluctuation fields maintain mean, variance, and covariance information (obtained from the initial RANS solution) in the long-time average. Morkovin's hypothesis of negligible pressure and total-temperature fluctuations was used to obtain density and temperature fluctuation fields from the velocity fluctuations. Some calculations were performed without random forcing of the inflow profile; results were slightly inferior to those with random forcing, and as a result, the forcing procedure was used for all presented calculations. The recycling procedure described in the preceding section was not used for this case. Extrapolation boundary conditions were applied along the outflow boundaries (top and right side in Fig. 2), whereas no-slip, adiabatic wall boundary conditions were applied along all solid surfaces. Periodic boundary conditions were applied in the Z direction, as the flow is assumed to be spatially homogeneous in this direction.

Time-dependent calculations were run for 10.5 characteristic times to establish a statistically stationary state. (One characteristic time is defined as the time required for a freestream fluid particle to traverse the domain and is equal to 0.00043 s for the present conditions.) Statistics were then gathered for an additional seven characteristic times. A fixed time step of 1.5×10^{-7} s was used for the calculations. Three to six subiterations were required to reduce the residual at each physical time step two orders of magnitude. Time-dependent flow properties were averaged over the Z direction to yield nominally two-dimensional predictions.

Figure 3 presents a snapshot of velocity magnitude contours at the $Z = 0.0191$ m midplane. Spanwise contours at the locations A and B are also displayed. The dominant features of the flow are a free-shear layer over the cavity, which reattaches to form a turbulent boundary layer on the ramped portion of the cavity. A large recirculation zone behind the cavity leading edge is also present, as is a compression fan which coalesces into a shock wave downstream of the reattachment point. This case is considered statistically stationary in that the self-oscillating cycle typical of rectangular cavity flowfields was not observed in the experiment. This is caused in part by the shallow aft wall angle (20 deg), which redirects acoustic disturbances away from the front cavity wall. The initial growth of the shear layer is dominated by elongated Kelvin–Helmholtz structures, which are nominally two-dimensional. These structures break down in a highly three-dimensional fashion after reattachment. The size of the horseshoe vortices present in the boundary layer after reattachment is of the order of half of the domain width in the Z direction (about 0.75 cm).

Comparisons with the wall and mean profile data of Settles et al.[20] are shown in Figs. 4–7 for the baseline grid. The different models

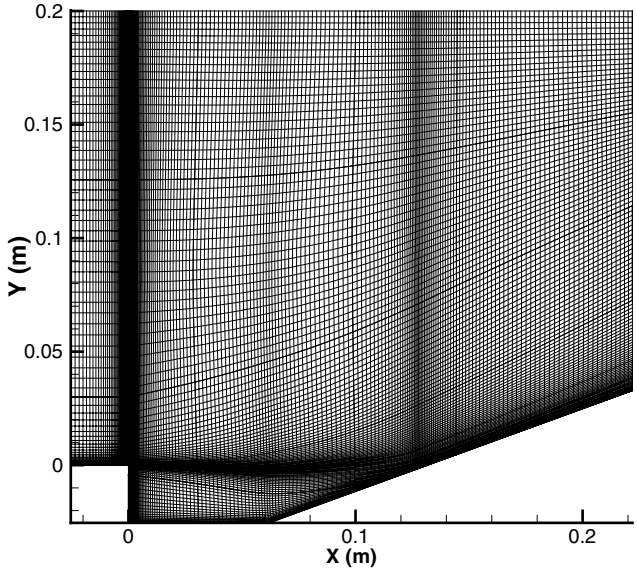

Fig. 2 X–Y grid for ramped-cavity configuration.

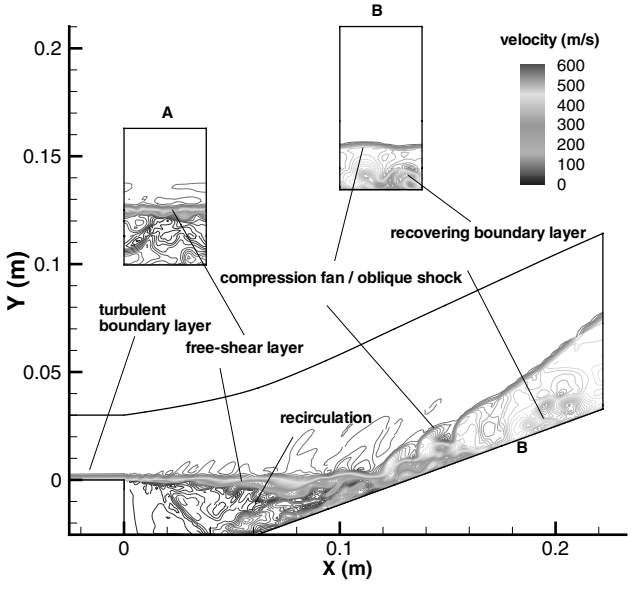

Fig. 3 Instantaneous velocity magnitude (m/s) contours (ramped-cavity configuration).

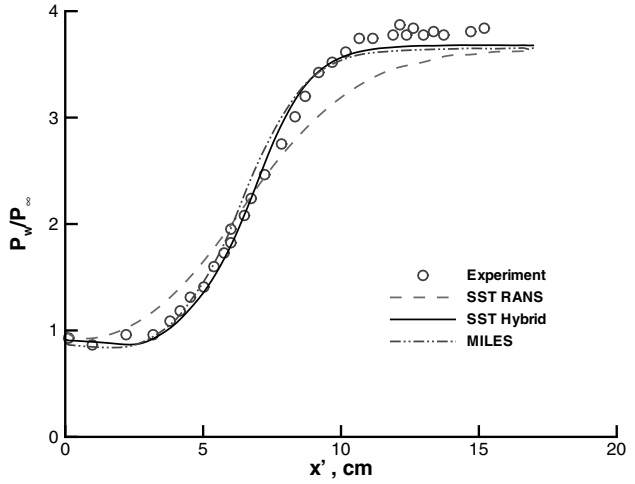

Fig. 4 Wall-pressure (N/m^2) distribution (ramped-cavity configuration).

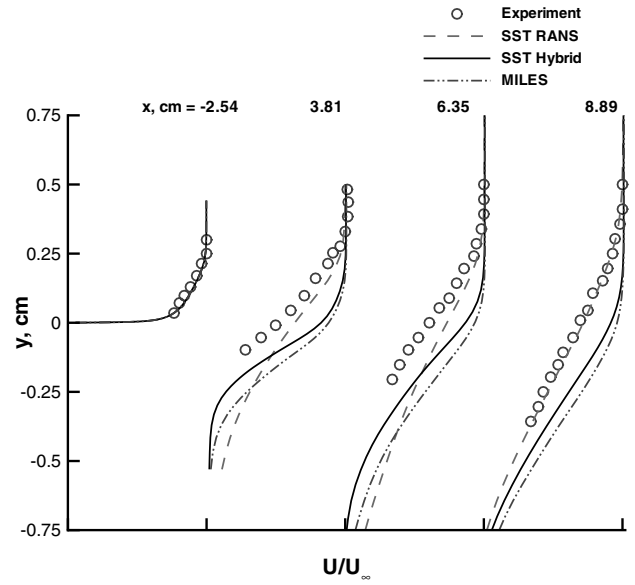

Fig. 5 Velocity profiles in shear layer (ramped-cavity configuration). Note: each major tick mark on the *X* axis represents one unit.

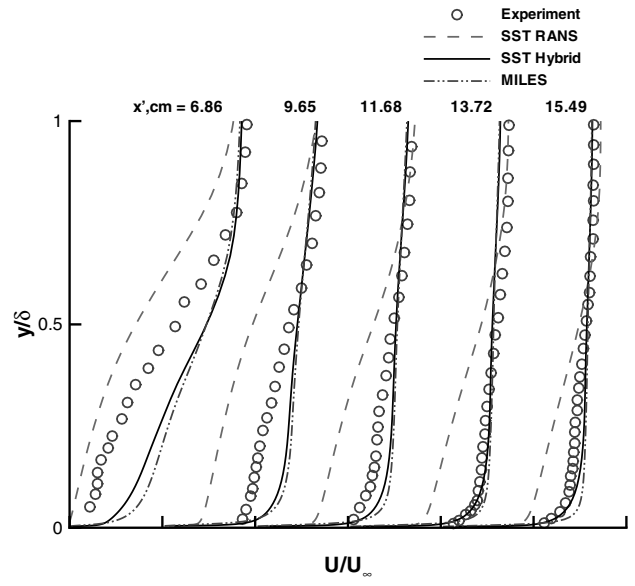

Fig. 6 Velocity profiles in recovery region (ramped-cavity configuration). Note: each major tick mark on the *X* axis represents one half-unit.

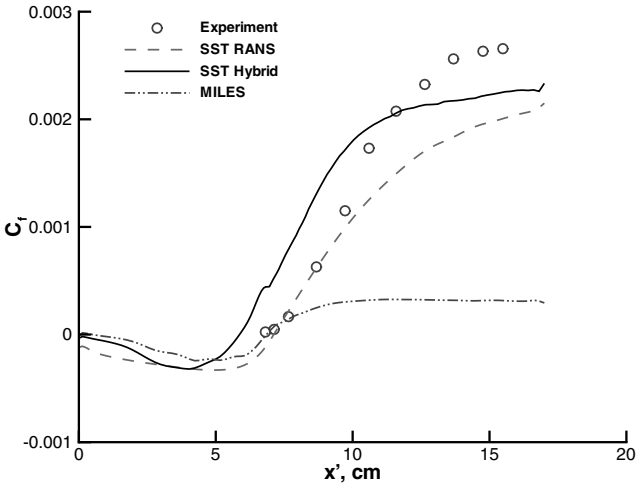

Fig. 7 Skin-friction distribution (ramped-cavity configuration).

used are the Menter SST model (two-dimensional steady RANS), the hybrid model, and the MILES approach. Figure 4 presents wall-pressure comparisons on the ramped portion of the cavity. The midpoint of the pressure rise coincides roughly with the reattachment location, whereas the rise itself is indicative of the rate of recovery of the boundary layer downstream of reattachment. As shown, both the hybrid and MILES models provide good predictions, whereas the RANS model results in a more gradual recompression.

Figure 5 presents mean velocity profiles within the shear layer prior to reattachment. Here, both the hybrid and MILES models underestimate the initial growth of the shear layer and the degree of its displacement into the outer core flow. The RANS approach provides generally better predictions further away from the cavity leading edge but overestimates the initial spreading rate of the shear layer. Figure 6 presents velocity profiles in the recovery region. Profiles in the recovery region correspond to particular locations along the ramp, measured from the juncture of the cavity and the ramp.[20,21] The distance is extracted normal to the wall and is nondimensionalized by the experimentally measured boundary-layer thickness, while the local velocity is normalized by the freestream velocity. Both of the time-dependent models perform reasonably well in predicting the recovery of the boundary layer following reattachment, but neither properly captures the velocity profile just downstream of reattachment. The MILES results overpredict the velocity distribution in the inner part of the boundary layer but are otherwise similar to those of the hybrid model. The RANS results consistently underestimate the rate of recovery of the boundary layer, with predicted velocity levels well below those measured in the inner part of the boundary layer. This response is typical of RANS models in postseparation recovery regions, and the success of the time-dependent models in overcoming this tendency is encouraging.

Figure 7 compares predicted skin-friction distributions along the ramp with the measured distribution from Ref. 20. The reattachment point is predicted accurately by the Menter SST model and by the MILES approach, but the hybrid model predicts reattachment as occurring farther upstream. Nevertheless, the hybrid model predicts the rate of increase in skin friction in the recovery region reasonably well, while the Menter SST model underpredicts both the rate and the peak value. The MILES predictions are more indicative of a laminar flow, rather than a turbulent one. The failure of the MILES approach is not that surprising, as the grid distributions in the near-wall region are too coarse in the *X* and *Z* directions to capture the eddy structure properly. Given this, one can view the hybrid model as providing the essential elements of a wall function-type closure for the log layer and below to an otherwise LES description of the flow.

Figures 8 and 9 provide an indication of the effects of doubling the spanwise Z extent of the domain while keeping the mesh spacing in the *Z* direction constant. As indicated, the predictions provided by

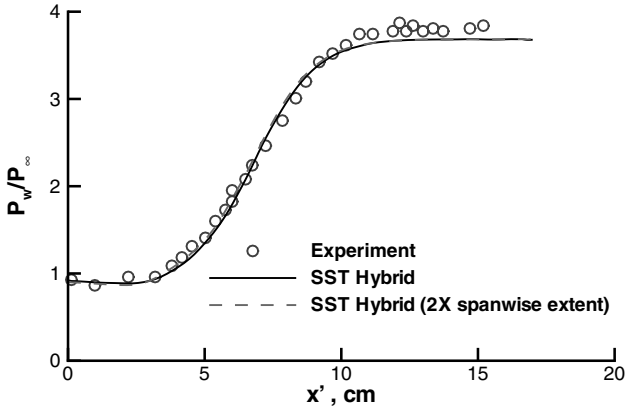

Fig. 8 Wall-pressure distribution: effect of spanwise domain extent (ramped-cavity configuration).

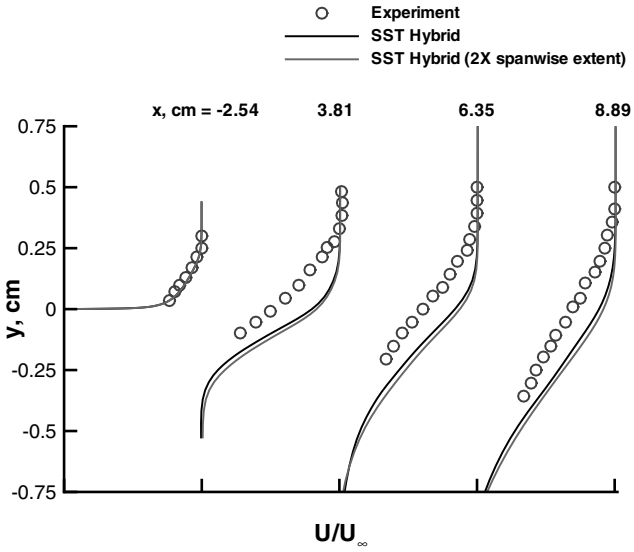

Fig. 9 Velocity profiles in shear layer: effect of spanwise domain extent (ramped-cavity configuration). Note: each major tick mark on the *X* axis represents one unit.

the hybrid model are relatively insensitive to the spanwise domain extent. Similar results (not shown) are found for the predictions of the velocity field and skin friction in the recovery region.

The results just presented indicate that the time-dependent models are not that successful in predicting the structure of the shear layer. One reason might be the absence of the inflow boundary recycling procedure, which, if applied, would result in more structural content in the incoming boundary layer. Another reason might be insufficient streamwise grid refinement, which can delay the development and breakdown of nominally two-dimensional Kelvin–Helmholtz structures. Figures 10–13 illustrate the effects of doubling the streamwise grid resolution downstream of the cavity leading edge on mean-flow predictions for the hybrid and the MILES models. Figure 10 shows that the wall-pressure distributions are relatively insensitive to grid refinement for the hybrid model but degrade slightly for MILES. In contrast, Figs. 12 and 13 show that the refined MILES calculation now captures the shear-layer spreading rate more precisely and provides better predictions of the velocity profile just downstream of the reattachment point. The hybrid-model predictions are less sensitive to mesh refinement but do show some slight improvements. One reason for the hybrid model's relative insensitivity to grid refinement for this case is illustrated in the instantaneous eddy viscosity contours of Fig. 14. The eddy viscosity is normalized by the molecular viscosity in the figure. Though the shear layer and the outer part of the recovering boundary layer are treated as LES (small eddy viscosity values), the majority of the recirculation zone

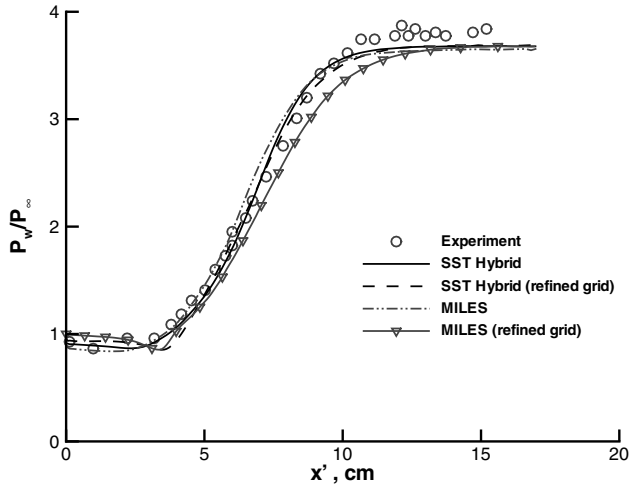

Fig. 10 Wall-pressure distribution: effect of streamwise grid refinement (ramped-cavity configuration).

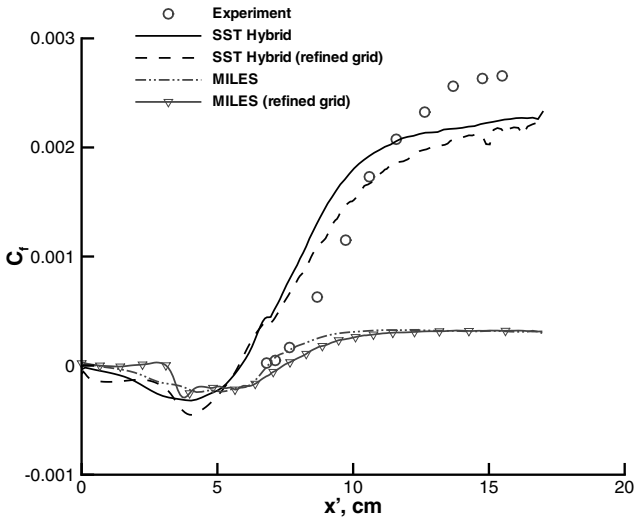

Fig. 11 Skin-friction distribution: effect of streamwise grid refinement (ramped-cavity configuration).

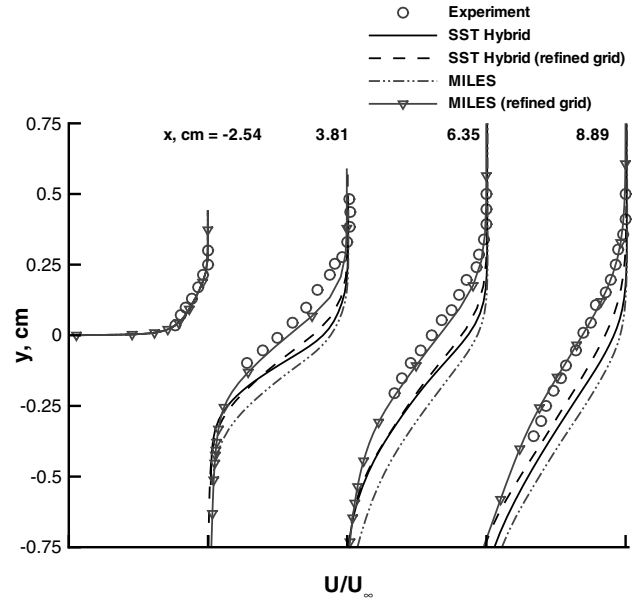

Fig. 12 Velocity profiles in shear layer: effect of streamwise grid refinement (ramped-cavity configuration). Note: each major tick mark on the *X* axis represents one unit.

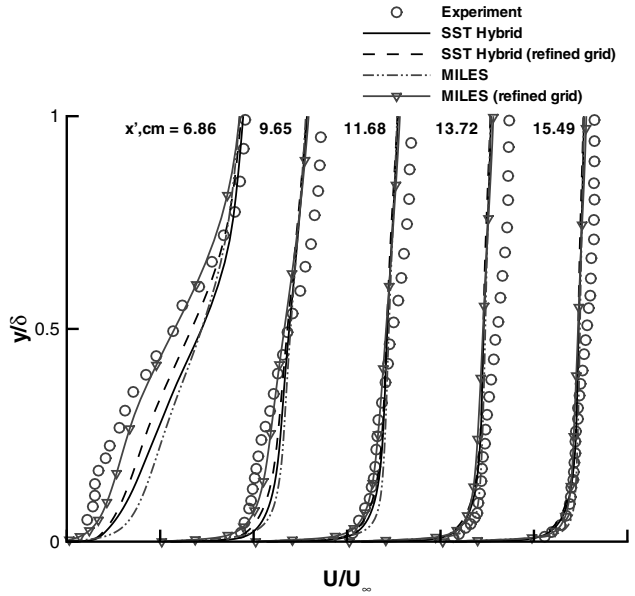

Fig. 13 Velocity profiles in recovery region: effect of streamwise grid refinement (ramped-cavity configuration). Note: each major tick mark on the *X* axis represents one half-unit.

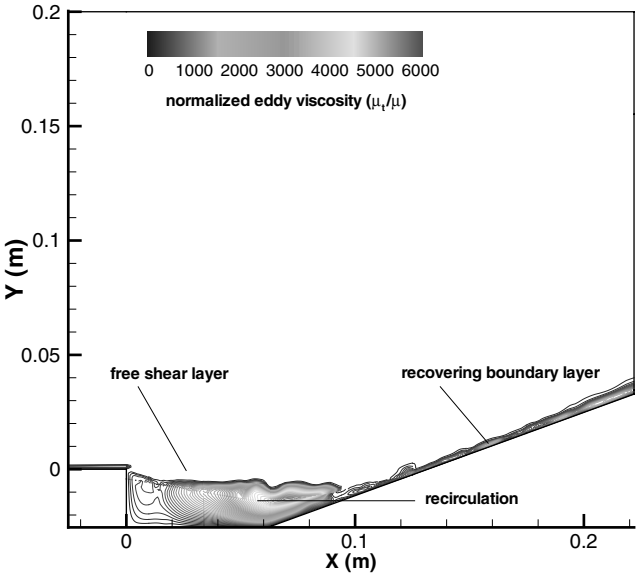

Fig. 14 Instantaneous normalized eddy viscosity (ramped-cavity configuration).

is modeled as RANS. This means that the quality of the results in this region will depend on the ability of the Menter SST model to predict recirculating flows. As shown in our earlier study,[17] the positioning of the "line of demarcation" between LES and RANS is sensitive to the constant C_d in Eq. (1). Higher values for C_d result in less production of subgrid turbulence kinetic energy, which leads to smaller values of the argument ζ in Eq. (5) and a shift in the blending function toward the walls. As shown later, one consequence of this shift is a reduction in the ability of the hybrid model to predict the skin friction accurately. The counterpoint is illustrated in Fig. 12, where the blending function is positioned too far out to enable good predictions of the shear-layer structure. The MILES approach responds much better to mesh refinement than the hybrid model, indicating that with sufficient grid resolution only very minimal levels of eddy viscosity appear to be necessary away from solid surfaces. As shown in Fig. 11, skin-friction predictions do not improve with mesh refinement for MILES, indicating that some type of RANS closure is still necessary for the near-wall flow.

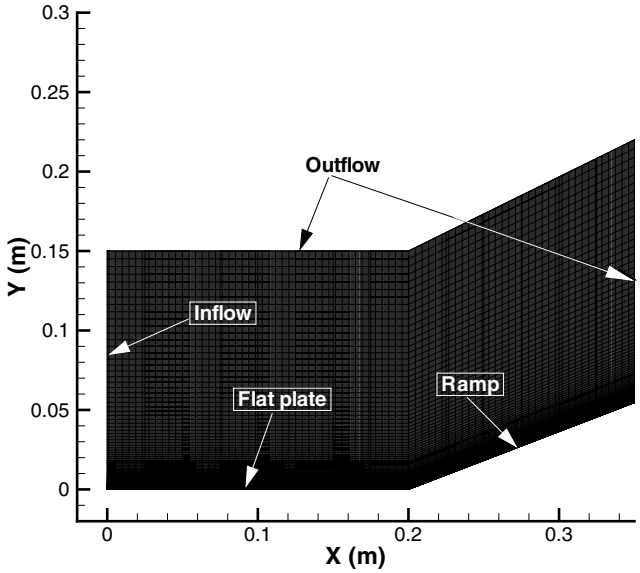

Fig. 15 *X–Y* grid for compression-ramp configuration.

20-Deg Compression Corner

The next set of simulations focuses on the 20-deg compression-corner flowfield experimentally mapped by Horstman et al.[22] and Settles and Dodson.[23] Figure 15 shows a two-dimensional view of the computational grid. This geometry consists of a flat plate that extends 0.2 m from the inflow plane, followed by a 20-deg compression ramp. The three-dimensional grid used for this case consists of $449 \times 129 \times 65$ points, which are decomposed into 84 smaller blocks for mapping onto the IBM SP-2 architecture. The grid extends 0.0783 m in the Z direction and is clustered in the Y direction to the flat plate and ramp. The grid spacing is uniform in the X and Z directions. Inflow conditions were obtained by calculating two-dimensional flow over a flat plate until the boundary-layer properties just upstream of the interaction matched the experimental values. The nominal inflow Mach number, pressure, and temperature are 2.79, 26,001 Pa, and 100.8 K, respectively, yielding a Reynolds number per meter of 7.2×10^7. The inflow boundary-layer thickness is 2.7 cm. As before, initial conditions for the hybrid simulations were obtained by solving the flowfield in two dimensions using the Menter SST model. In the initial step of the time-dependent simulations, a random perturbation, constructed based on the procedure presented in Ref. 28, was applied to all flow variables to enable a more rapid formation of three-dimensional structures.

Extrapolation boundary conditions were applied along the outflow boundaries (top and right sides in Fig. 15). Standard no-slip, adiabatic wall boundary conditions were applied along the flat plate/ramp surface (bottom side in Fig. 15). Periodic boundary conditions were applied in the Z direction for the hybrid simulations, as the flow is assumed to be spatially homogeneous in that direction. The inflow boundary conditions were either fixed at the mean values resulting from the RANS calculation or treated as time dependent using the recycling procedure described earlier.

Hybrid simulations with fixed inflow boundary conditions were run for 4.8 characteristic times (one characteristic time equals 0.00062 s for this case) to establish a statistically stationary state. Simulations with time-dependent inflow boundary conditions reached the statistically stationary state more quickly, taking 4.1 characteristic times. Both cases were run an additional 4.8 characteristic times to collect statistics. A time step of 7.5×10^{-8} s was used for the first few characteristic times. A larger time step of 1.5×10^{-7} s was used at later times to speed up the the time-averaging process. Time-dependent flow properties were spatially and temporally averaged in the same manner as described for the ramped-cavity case.

Snapshots of three-dimensional axial velocity and pressure contours for the compression ramp flowfield are shown in Figs. 16 and 17. Dominant features of this flowfield include an incoming

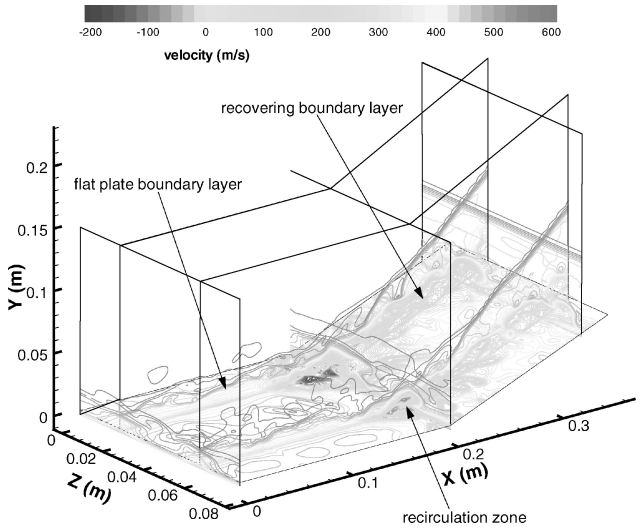

Fig. 16 Three-dimensional instantaneous axial velocity contours (compression corner).

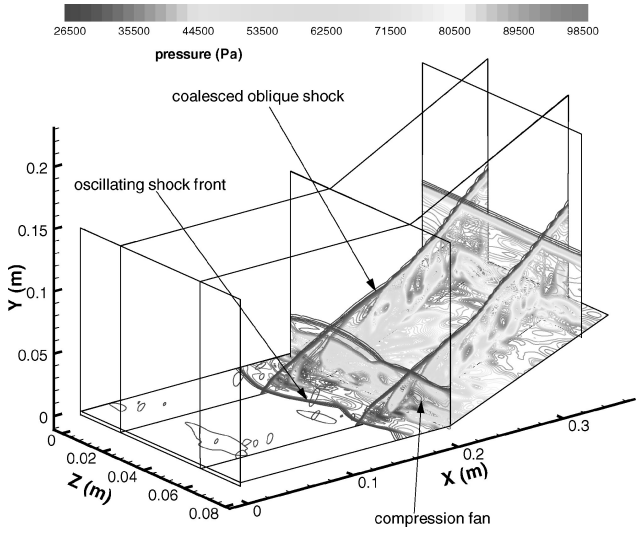

Fig. 17 Three-dimensional instantaneous pressure contours (compression corner).

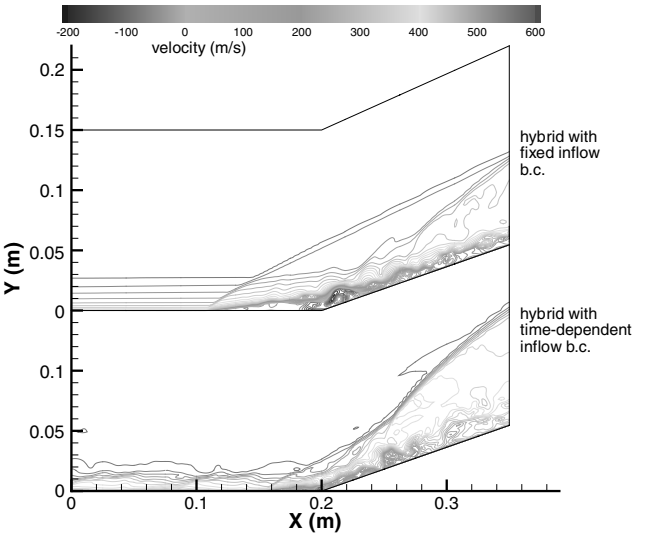

Fig. 18 Effects of inflow boundary conditions on instantaneous axial velocity: *X*–*Y* slice.

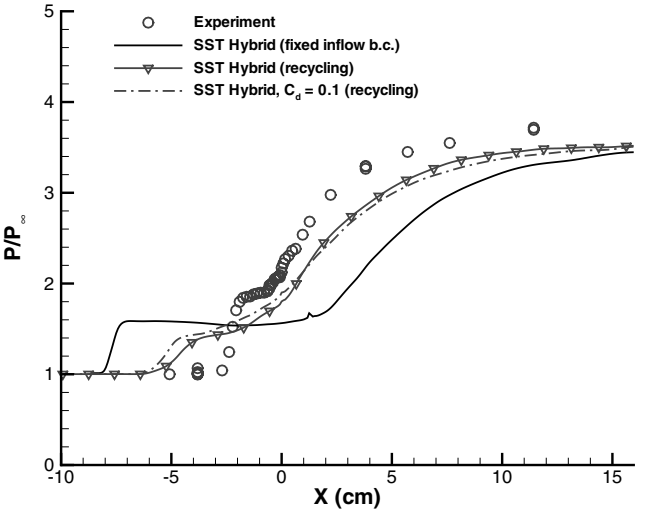

Fig. 19 Wall-pressure distributions (compression corner).

turbulent boundary layer on the flat plate, an oblique shock that induces a region of flow separation in the vicinity of ramp corner, and a recovering boundary layer on the ramp surface. Note the fluctuating wave front of the shock system in the spanwise direction shown in Fig. 17. This phenomenon has also been observed in experimental works.[31] Characteristics of the shock-wave/boundary-layer interaction present in this flow include the delayed response of the Reynolds stress to the initial shock-induced disturbance, the eventual rapid amplification of the Reynolds stress through the interaction region, and its relaxation toward an equilibrium state as the flow moves downstream.[32]

Figure 18 presents the effects of the different treatments of inflow boundary conditions on the hybrid simulation results. The contour plot on the top shows results from the hybrid model with fixed boundary conditions imposed at the inflow. A RANS-type boundary layer is seen developing from the inflow. As this boundary layer encounters the separation shock, a wakelike structure forms above the separation region. The blending function senses this as a transition into a free-shear layer and thus lowers the eddy viscosity. The SST component of Menter's model also helps lower the RANS eddy viscosity in the vicinity of the separation shock, where the local strain rate exceeds the turbulence frequency ω. This rapid reduction in eddy viscosity eventually results in a shift to LES mode, and the recovering boundary layer on the ramp contains clear evidence of large-scale structures. This shift does not occur instantaneously, and upstream of the corner the computed boundary layer cannot maintain its energy level and becomes vulnerable to the adverse pressure gradient induced by the shock system. Thus, the pocket of reversed flow upstream of the corner enlarges over time. The other treatment uses the recycling procedure described in the earlier section. The contours on the bottom show that the incoming boundary layer now contains time-resolved large-scale structures as a result of recycling the fluctuation field back into the inflow. These structures appear to maintain more of their energy content as the model shifts from a RANS to a LES mode of operation, and the result is less separation upstream of the corner.

The time-averaged results from these two simulations (run with $C_d = 0.01$) are compared with Settles's experimental data[22,23] in Figs. 19–22. Results from a hybrid simulation with a higher destruction constant ($C_d = 0.1$) are also shown, as are RANS results using the Menter SST model. Figure 19 shows the pressure distributions along the wall surface. In this and subsequent figures, the X coordinate is the distance measured along the ramp surface and its origin ($X = 0.0$ cm) is taken at the flat-plate/ramp juncture. The initial rise in pressure corresponds to the positioning of the separation shock. The hybrid model with fixed inflow conditions greatly overpredicts the extent of axial separation. The hybrid models with fluctuation recycling provide a definite improvement but still overpredict the upstream extent of separation. The extent of the initial

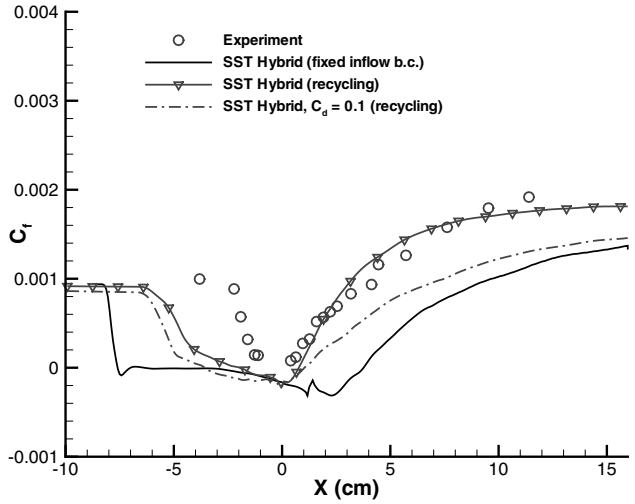

Fig. 20 Skin-friction distributions (compression corner).

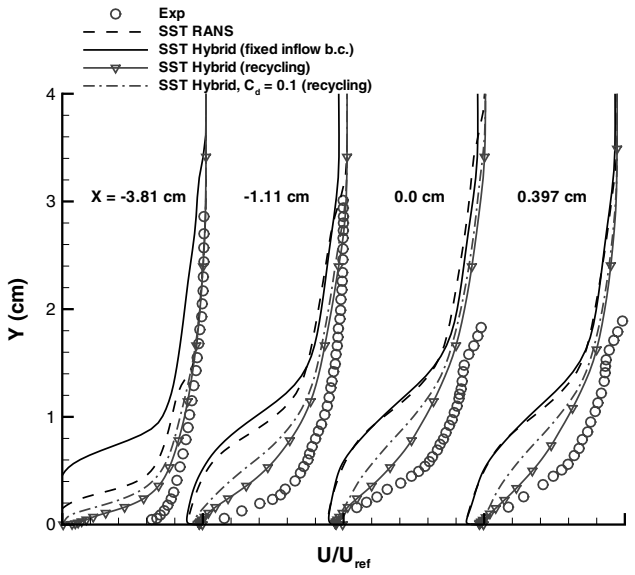

Fig. 21 Velocity profiles in vicinity of ramp apex (compression corner). Note: each major tick mark on the *X* axis represents one unit.

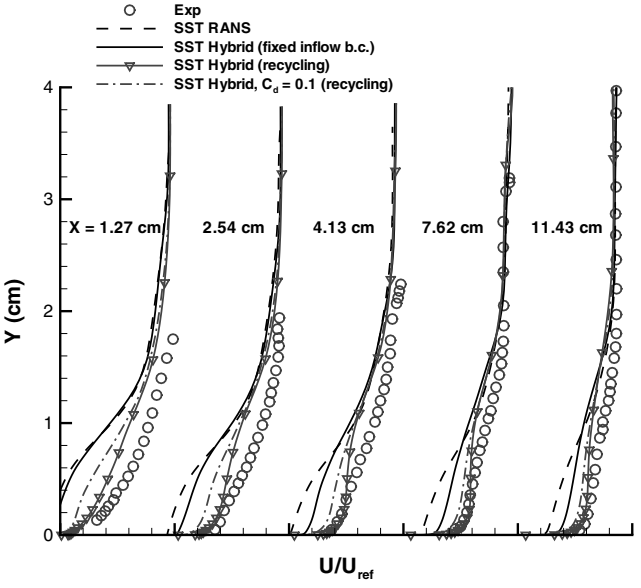

Fig. 22 Velocity profiles in recovery region (compression corner). Note: each major tick mark on the *X* axis represents one unit.

pressure rise indicates the strength of the separation shock, and all of the time-dependent models predict a weaker shock than indicated in the experimental data. A compression fan forms downstream of the separation shock, as indicated by a gradual rise in pressure on the ramp surface. All of the models capture the rate of pressure rise reasonably well, but the rise itself takes place farther downstream than indicated in the experimental data. Differences between predictions of the hybrid models run with $C_d = 0.1$ and 0.01 are seen to be minor. The RANS model also overpredicts the extent of axial separation but predicts the separation-shock pressure rise better than the time-dependent models.

Figure 20 shows the skin-friction distributions. All of the time-dependent models underpredict the skin-friction levels in the incoming boundary layer. All of the models predict the drop in skin friction as occurring further upstream than indicated in the experimental data, with the hybrid model with fixed inflow boundary conditions separating the earliest. Both recycling hybrid models predict the reattachment point quite well, while the other models locate the reattachment point farther downstream. The rise in skin friction downstream of reattachment is indicative of the rate of recovery of the inner part of the boundary layer. The recycling hybrid model with $C_d = 0.01$ predicts an excellent rate of recovery. The same model run with $C_d = 0.1$ produces lower skin-friction levels in the recovery region because of a smaller RANS component in this region. This is caused by lower turbulent kinetic energy levels and the resulting shift in the blending function toward the wall [Eq. (4)]. The RANS model displays the worst response in terms of skin-friction recovery. However, RANS predictions obtained without using the SST modification are quite good for this flow and, in fact, underestimate the axial extent of separation.[17]

Figures 21 and 22 present the velocity profiles in the vicinity of ramp corner and the recovery region on the ramp, respectively. In both figures, the velocity profiles are extracted normal to the surface and are normalized by experimentally measured reference velocities. General shapes of the profiles are captured in the vicinity of ramp corner by the recycling hybrid models, though the velocity levels are well underpredicted. This is because of the inaccurate prediction of the separation shock location, which leads to a premature loss of momentum in the inner part of the boundary layer. The results are not satisfactory in this region, but they are nevertheless better than the predictions of the hybrid model with fixed inflow conditions and the Menter SST model. It is interesting that the Menter SST predictions of the wake-like response above the backflow region are very similar to those of the fixed-inflow hybrid model. This indicates that the latter is operating primarily in RANS mode in this region of the flow (see also Fig. 18). In the recovery region, however, the near-wall velocity levels are captured very well by the recycling hybrid model with $C_d = 0.01$. Velocity levels in the outer part of the recovering boundary layer are slightly underpredicted. The higher C_d case displays an underprediction of velocity levels in the near-wall region. This effect reflects the observations made earlier regarding the positioning of the instantaneous LES/RANS juncture and its effect on near-wall predictions. The velocity field corresponding to the fixed-inflow hybrid model does not recover as rapidly as that of the recycling hybrid models, but nevertheless, the rate of recovery is higher than that predicted by the RANS model. These results indicate that once the hybrid models shift to a primarily LES mode of operation in the outer part of the boundary layer they are capable of capturing the rapid amplification of the Reynolds stress that leads to rapid recovery.

Conclusions

An approach for conducting hybrid large-eddy/Reynolds-averaged simulations of high-speed, shock-separated flows has been presented in this work. The approach uses a distance-dependent blending function to shift the turbulence closure from the Menter shear-stress-transport Reynolds-averaged Navier–Stokes (SST RANS) model near solid surfaces to a one-equation subgrid model away from solid surfaces.

Results have been obtained for two cases: Mach 3 flow over a ramped-cavity configuration and Mach 3 flow over a 20-deg

compression corner. The ramped-cavity simulations indicate that, with sufficient mesh refinement, the hybrid procedure captures the structure of the developing shear layer and the recovering boundary layer reasonably well. Simulations performed using a MILES approach also respond well with grid refinement, indicating that with sufficient resolution, only very minimal levels of eddy viscosity are necessary away from solid surfaces. A shift to RANS modeling near solid surfaces appears necessary to predict near-wall properties accurately, and the instantaneous location of the RANS/LES juncture within the boundary layer (which is affected by the choice of model constants) is an important parameter in this prediction.

The compression-corner simulations indicate that it is necessary to account for the presence of large-eddy structures in the inflow boundary layer to improve predictions for wall-bounded, separated flows. Even with this modification, predictions of the upstream extent of axial separation are not completely satisfactory; however, the hybrid models do excel in predicting the structure of the recovering boundary layer downstream of reattachment. This feature is a major advantage over purely RANS models, which generally fail to predict the levels of turbulent fluctuation amplification necessary to produce a rapid recovery. One can conjecture, then, that hybrid LES/RANS procedures can achieve even more success for flows with multiple shock-wave/boundary-layer interactions.

Future work must assess the effects of combining the hybridization strategy with other RANS turbulence models, the development of alternative blending functions, and the application of this technology to more complex interactions.

Acknowledgments

This research was sponsored by Taitech, Inc., under Contract F33615-00-C-2017. IBM SP-2 computer time was provided by a grant from the North Carolina Supercomputing Center.

References

[1]Spalart, P. R., Jou, W.-H., Strelets, M., and Allmaras, S. R., "Comments on the Feasibility of LES for Wings, and on a Hybrid RANS/LES Approach," First AFOSR International Conf. on DNS/LES, Aug. 1997.

[2]Nikitin, N. V., Nicoud, F., Wasistho, B., Squires, K. D., and Spalart, P. R., "An Approach to Wall Modeling in Large-Eddy Simulations," *Physics of Fluids*, Vol. 12, No. 7, 2000, pp. 1629–1632.

[3]Spalart, P. R., "Trends in Turbulence Treatments," AIAA Paper 2000-2306, June 2000.

[4]Strelets, M., "Detached Eddy Simulation of Massively Separated Flows," AIAA Paper 2001-0879, Jan. 2001.

[5]Forsythe, J. R., Hoffmann, K. A., and Dietiker, J.-F. "Detached-Eddy Simulation of a Supersonic Axisymmetric Base Flow with an Unstructured Solver," AIAA Paper 2000-2410, June 2000.

[6]Travin, A., Shur, M., Strelets, M., and Spalart, P., "Detached Eddy Simulations past a Circular Cylinder," *Flow, Turbulence, and Combustion*, Vol. 63, No. 1–4, 1999, pp. 293–313.

[7]Bush, R., and Mani, M., "A Two-Equation Large-Eddy Stress Model for High Sub-Grid Shear," AIAA Paper 2001-2561, June 2001.

[8]Speziale, C. G., "Turbulence Modeling for Time Dependent RANS and VLES: A Review," *AIAA Journal*, Vol. 36, No. 2, 1998, pp. 173–184.

[9]Arunajatesan, S., Sinha, N., and Menon, S., "Towards Hybrid LES-RANS Computations of Cavity Flowfields," AIAA Paper 2000-0401, Jan. 2000.

[10]Arunajatesan, S., and Sinha, N., "Unified Unsteady RANS-LES Simulations of Cavity Flowfields," AIAA Paper 2001-0516, Jan. 2001.

[11]Zhang, H.-L., Bachman, C. R., and Fasel, H. F., "Application of a New Methodology for Simulations of Complex Turbulent Flows," AIAA Paper 2000-2535, June 2000.

[12]Batten, P., Goldberg, U., and Chakravarthy, S., "Sub-Grid Turbulence Modeling for Unsteady Flow with Acoustic Resonance," AIAA Paper 2000-0473, Jan. 2000.

[13]Forsythe, J. R., Squires, K. D., Wurtzler, K. E., and Spalart, P. R., "Detached-Eddy Simulation of Fighter Aircraft at High Alpha," AIAA Paper 2002-0591, Jan. 2002.

[14]Georgiadis, N. J., Alexander, J. I. D., and Reshotko, E., "Hybrid Reynolds-Averaged Navier–Stokes/Large-Eddy Simulations of Supersonic Turbulent Mixing," *AIAA Journal*, Vol. 41, No. 2, 2003, pp. 218–229.

[15]Baurle, R. A., Tam, C.-J., Edwards, J. R., and Hassan, H. A., "Hybrid Simulation Approach for Cavity Flows: Blending, Algorithm, and Boundary Treatment Issues," *AIAA Journal*, Vol. 41, No. 8, 2003, pp. 1463–1480.

[16]Fan, T. C., Tian, M., Edwards, J. R., Hassan, H. A., and Baurle, R. A., "Validation of a Hybrid Reynolds-Averaged/Large-Eddy Simulation Method for Simulating Cavity Flameholder Configurations," AIAA Paper 2001-2929, June 2001.

[17]Fan, T. C., Xiao, X., Edwards, J. R., Hassan, H. A., and Baurle, R. A., "Hybrid LES/RANS Simulation of a Mach 3 Shock Wave/Boundary Layer Interaction," AIAA Paper 2003-0080, Jan. 2003.

[18]Xiao, X., Edwards, J. R., Hassan, H. A., and Baurle, R. A., "Inflow Boundary Conditions for Hybrid Large Eddy/Reynolds-Averaged Navier–Stokes Simulations," *AIAA Journal*, Vol. 41, No. 8, 2003, pp. 1481–1489.

[19]Menter, F. R., "Two Equation Eddy Viscosity Turbulence Models for Engineering Applications," *AIAA Journal*, Vol. 32, No. 8, 1994, pp. 1598–1605.

[20]Settles, G. S., Williams, D. R., Baca, B. K., and Bogdonoff, S. M., "Reattachment of a Compressible Turbulent Free Shear Layer," *AIAA Journal*, Vol. 20, No. 1, 1982, pp. 60–67.

[21]Horstman, C. C., Settles, G. S., Williams, D. R., and Bogdonoff, S. M., "A Reattaching Free Shear Layer in Compressible Turbulent Flow," *AIAA Journal*, Vol. 20, No. 1, 1982, pp. 79–85.

[22]Horstman, C. C., Settles, G. S., Vas, I. E., Bogdonoff, S. M., and Hung, C. M., "Reynolds Number Effects on Shock-Wave Turbulent Boundary Layer Interactions—A Comparison of Numerical and Experimental Results," AIAA Paper 77-42, Jan. 1977.

[23]Settles, G. S., and Dodson, L. J., " Hypersonic Shock/Boundary Layer Interaction Database," NASA CR-177577, April 1991.

[24]Yoshizawa, A., and Horiuti, K., "A Statistically-Derived Subgrid Scale Kinetic Energy Model for Large-Eddy Simulation of Turbulent Flows," *Journal of the Physical Society of Japan*, Vol. 54, No. 8, 1985, pp. 2834–2837.

[25]Boris, J. P., Grinstein, F. F., Oran, E. S., and Kolbe, R. L., "New Insights into Large Eddy Simulation," *Fluid Dynamics Research*, Vol. 10, Dec. 1992, pp. 199–228.

[26]Fureby, C., Nilsson, Y., and Anderson, K., "Large Eddy Simulation of Supersonic Base Flow," AIAA Paper 99-0426, Jan. 1999.

[27]Urbin, G., Knight, D., and Zheltovodov, A. A., "Large Eddy Simulation of a Supersonic Boundary Layer Using an Unstructured Grid," *AIAA Journal*, Vol. 29, No. 7, 2001, pp. 1288–1295.

[28]Norris, J. W., and Edwards, J. R., "Large-Eddy Simulation of High-Speed, Turbulent Diffusion Flames with Detailed Chemistry," AIAA Paper 97-0370, Jan. 1997.

[29]Suresh, A., and Huynh, H. T., "Numerical Experiments on a New Class of Nonoscillatory Schemes," AIAA Paper 92-0421, Jan. 1992.

[30]Edwards, J. R., "A Low-Diffusion Flux-Splitting Scheme for Navier–Stokes Calculations," *Computers and Fluids*, Vol. 26, No. 6, 1997, pp. 635–659.

[31]Dolling, D. S., and Murphy, M. T., "Unsteadiness of the Separation Shock Wave Structure in a Supersonic Compression Ramp Flowfield," *AIAA Journal*, Vol. 23, No. 12, 1983, pp. 1628–1634.

[32]Smits, A. J., and Muck, K.-C., "Experimental Study of Three Shock Wave/Turbulent Boundary Layer Interactions," *Journal of Fluid Mechanics*, Vol. 182, 1987, pp. 291–314.

B. Hassan
Associate Editor